Research article

Electric field and viscous fluid polarity effects on capillary-driven flow dynamics between parallel plates

Rizwan Ul Hassan [a], Shaheer Mohiuddin Khalil [b], Saeed Ahmed Khan [b,c], Joonkyeong Moon [b], Dae-Hyun Cho [d,e,*], Doyoung Byun [b,**]

[a] *Department of Mechanical Engineering, Yonsei University, 50 Yonsei-ro, Seodaemun-gu, Seoul, 03722, Republic of Korea*
[b] *Department of Mechanical Engineering, Sungkyunkwan University, Suwon 16419, Republic of Korea*
[c] *Department of Electrical Engineering, Sukkur IBA University, Sukkur 65200, Pakistan*
[d] *Department of Mechatronics Engineering, Gyeongsang National University, 33 Dongjin-ro, Jinju, Gyeongsangnam-do, 52725, Republic of Korea*
[e] *Department of Energy System Engineering, Gyeongsang National University, 501 Jinjudae-ro, Jinju, Gyeongsangnam-do, 52828, Republic of Korea*

A B S T R A C T

—Micropumps have attracted considerable interest in micro-electro-mechanical systems (MEMS), microfluidic devices, and biomedical engineering to transfer fluids through capillaries. However, improving the sluggish capillary-driven flow of highly viscous fluids is critical for commercializing MEMS devices, particularly in underfill applications. This study investigated the behavior of different viscous fluid flows under the influence of capillary and electric potential effects. We observed that upon increasing the electric potential to 500 V, the underfill flow length of viscous fluids increased by 45% compared to their capillary flow length. To explore the dynamics of underfill flow under the influence of an electric potential, the polarity of highly viscous fluids was altered by adding NaCl. The results indicated an increase of 20–41% in the underfill flow length of highly viscous conductive fluids (0.5–4% NaCl additives in glycerol) at 500 V compared to that at 0 V. The underfill viscous fluid flow length improved under the electric potential effect owing to the polarity across the substance and increased permittivity of the fluid. A time-dependent simulation, which included a quasi-electrostatic module, level set module, and laminar two-phase flow, was executed using the COMSOL Multiphysics software to analyze the effect of the external electric field on the capillary-driven flow. The numerical simulation results agreed well with the experimental data, with an average deviation of 4–7% at various time steps for different viscous fluids. Our findings demonstrate the potential of utilizing electric fields to control the capillary-driven flow of highly viscous fluids in underfill applications.

1. Introduction

For decades, underfill materials have been transferred into chip-to-substrate standoffs using capillary-driven flow [1–6]. Conventional underfill materials used in capillary-driven flow are composed of thermoset epoxy polymers with silica filler particles [7,8],

---

generally demonstrating a slow flow rate owing to their high viscosity. Hence, a complete filling of the chip-to-substrate standoff and shortening of the filling time have been regarded as technical challenges [9,10] in capillary-driven flow. Various studies have claimed that capillary-driven flow can be enhanced by modifying the surface wettability [11–14], driving pressure gradient [15], thermal stresses [16–18], and electric field effects [19–22].

In terms of wettability control, superhydrophobic coatings have been extensively explored to limit the contact area between the capillary wall and liquid [23–25]. Owing to the presence of micro/nanostructures, a nonzero flow exists at the solid-liquid boundary, enhancing slip-induced flow in low-viscosity fluids. However, an increase in the fluid viscosity can still increase the capillary filling time. In previous studies, researchers improved the capillary-driven flow of a highly viscous glycerol droplet; they noticed that the highly viscous glycerol flowed faster than water owing to deformation and air trapped within the micro/nanostructures of glass capillaries created by the superhydrophobic coatings. The spreading behavior was investigated on wettability patterned tracks for parametric modification of the liquid viscosity [26]. The findings revealed that the spreading morphologies of various viscous fluids were similar; however, highly viscous fluids required additional time to reach the end of the channel track. The capillary flow of different viscous fluids with varying surface wettabilities was analyzed to determine the capillary filling speed [14]. Consequently, all liquids demonstrated a reduced speed for low-surface-energy capillaries compared to high-surface-energy capillaries.

The pressurized underfilling technique was previously used to examine incomplete filling under capillary flow, and the impact of a pressurized flow on the underfill time was examined. The researchers found that while pressure increased the fluid flow, the filling speed decreased when the fluid came into contact with a larger area [27]. The pressurized fluid flow had a shorter filling time, requiring more precautions to ensure assembly and resistance against the pressure-induced flow to prevent failures during manufacturing [28]. Notably, the use of pressurized fluid can cause the mold fluid and flip-chip package to interact with each other, leading to package deformation or solder bump breakage.

In addition to the surface wettability and pressurized capillary flow, thermocapillary stresses can direct liquid micro streams along defined paths [29,30]. The thermocapillary method modifies the surface tension at one end of a liquid plug using heating devices outside the channel [31,32]. The temperature difference between the front and rear ends creates a capillary pressure gradient for liquid propulsion. Darhuber et al. investigated the effect of a thermal gradient on low viscosity fluid flow to develop a tunable and elegant technique for fluid transport [33] and observed that induced thermocapillary stresses appropriately steered microfluid streams along lithographically characterized pathways. Moreover, the migration behavior of liquid droplets on a metal substrate has been studied using the thermocapillary effect [34]. The findings indicate the need for developing a viable method for predicting the migration velocity as a function of the heat gradient, which can also increase the mechanical stress on the capillary wall. The flow of highly viscous fluids can also be increased by tilting the capillary channel [35]; however, this method has limitations because tilting is not feasible in several industrial processes.

In flip-chip packaging, the combination of the electrohydrodynamic (EHD) phenomenon with capillary systems has recently attracted the attention of several researchers [36–41]. The EHD phenomenon has attracted interest in fluid control at the nanoscale level, in addition to the processes mentioned above. EHD systems use electric fields to improve and control mass flow distribution [42–44]. The EHD phenomenon has been employed in several applications, including capillary pumping, improved heat transfer, and printed electronics [45–49]. The electric and magnetic forces significantly extend the fluid flow length and decrease void defects when the electrodes are in physical contact with the capillary walls. In previous studies, for multiphase electro-kinetics applications, pressure-driven movements of immiscible fluids were examined under an electric field [50], where the effects of surface potential and liquid conductivity on filling dynamics were found to enhance the fluid flow. The electric current increased when an electromagnetic field was applied to the capillary walls through the attached electrodes, reducing the filling time [51]. The influence of the polarization force on the liquid flow was demonstrated by EHD pumping for dielectric liquid flow in a microchannel [52]. Numerical studies on the polarization force showed a significant reduction in the encapsulant filling time and an improvement in the flow length in a micro-channel [53]. Although EHD pumping can increase the fluid flow speed, presumably, we could not find any literature investigating the flow of highly viscous and conductive fluids under the influence of the EHD phenomenon. The findings summarized in this section indicate that the limited flow rate of underfill materials can be countered only to a limited extent by altering the wettability, driving pressure gradient, thermal stresses, and electric field effects. Enhancing the slow speed of highly viscous fluids is still an important concern of industry which takes a longer time to complete the underfill process.

Herein, we utilized the electric potential effect to increase the underfill flow length of various viscous fluids exhibiting dynamic viscosities ranging from 0.0018 to 1.2 Pa s between parallel plates; the polarity of the viscous fluids under an electric field was also investigated. To verify the effect of the electric potential on the underfill flow length of viscous fluids, we recorded the change in flow length by varying the electrical potential from 0 to 500 V. The polarity of the highly viscous fluids was also altered by adding NaCl to glycerol to investigate the dynamics of underfill flow length under the influence of the electric potential. The electrocapillary number was studied to explore the effect of electric potential on the viscous and conductive fluid flow dynamics. The 3D simulation was also performed to analyze the viscous fluids flow dynamics under the electric potential effect. Considering the Maxwell stress effect in the EHD system, we compared our experimental results with theoretical and numerical models, which elucidated the dynamics of capillary filling in a small cylindrical tube [7].

2. Experimental setup

2.1. Materials and properties

Ethanol and deionized (DI) water were purchased from Daejung Chemicals and Materials (Siheung-Si, South Korea) to clean the surface of the glass (Duran Wheaton Kimble) Glycerol, methanol, and NaCl were purchased from Sigma–Aldrich (South Korea).

Ethylene glycol was obtained from FUJIFILM Wako Pure Chemical Corporation (Osaka, Japan). Nano NC in South Korea provided a 34-gauge plastic nozzle. A syringe pump (Chemyx Inc.) was used to maintain a steady flow during the experiment.

2.2. Microchannel fabrication, characterization, and experimental procedure

To adjust the capillary gap position (Fig. 1a), glass slides were diced to make a rectangular channel of (2×4 mm) and positioned horizontally; these slides could also move in the vertical (y) direction. A stainless steel-nozzle (34-gauge) was used to deliver liquid at a flow rate of 5.33×10^{-11} m^3/s through a syringe pump. A high-speed camera (Mini UX100, Photron) was used to capture the spreading behavior of the capillary fluid and fluid flow meniscus dynamics. A light-emitting diode (SPO Inc.) was connected to a coaxial zoom lens to visualize the meniscal phenomenon. Videos and images were captured at 50 frames/s, with a time step of 100 ms and a shutter speed of 1/5,000 s. An amplifier (10/40A high-voltage power amplifier, TREK, USA) and function generator (33220A, Keysight, USA) were used to supply direct-current (DC) voltages to the nozzle tip to investigate the spreading dynamics of viscous fluids under different electric fields. The data corresponding to the spreading behavior of the liquid between the parallel plates was scaled, analyzed, and cropped using the ImageJ software. Fig. 1b and c presents the schematic of the experimental setup and voltage effect, respectively, and the experimental parameters are listed in Table 1.

2.3. Analysis of physical characteristics of the fluid

We examined the viscous fluids conductivities using an electrical conductivity meter (DKK-TOA, Japan), and the contact angle between water and the substrate was measured using a droplet analyzer (Femtofab Co., Ltd.). A surface tension analyzer (DST 60A, South Korea) and a viscometer (ARES-G2, Rheometer, USA) were used to measure the surface tension and viscosity, respectively.
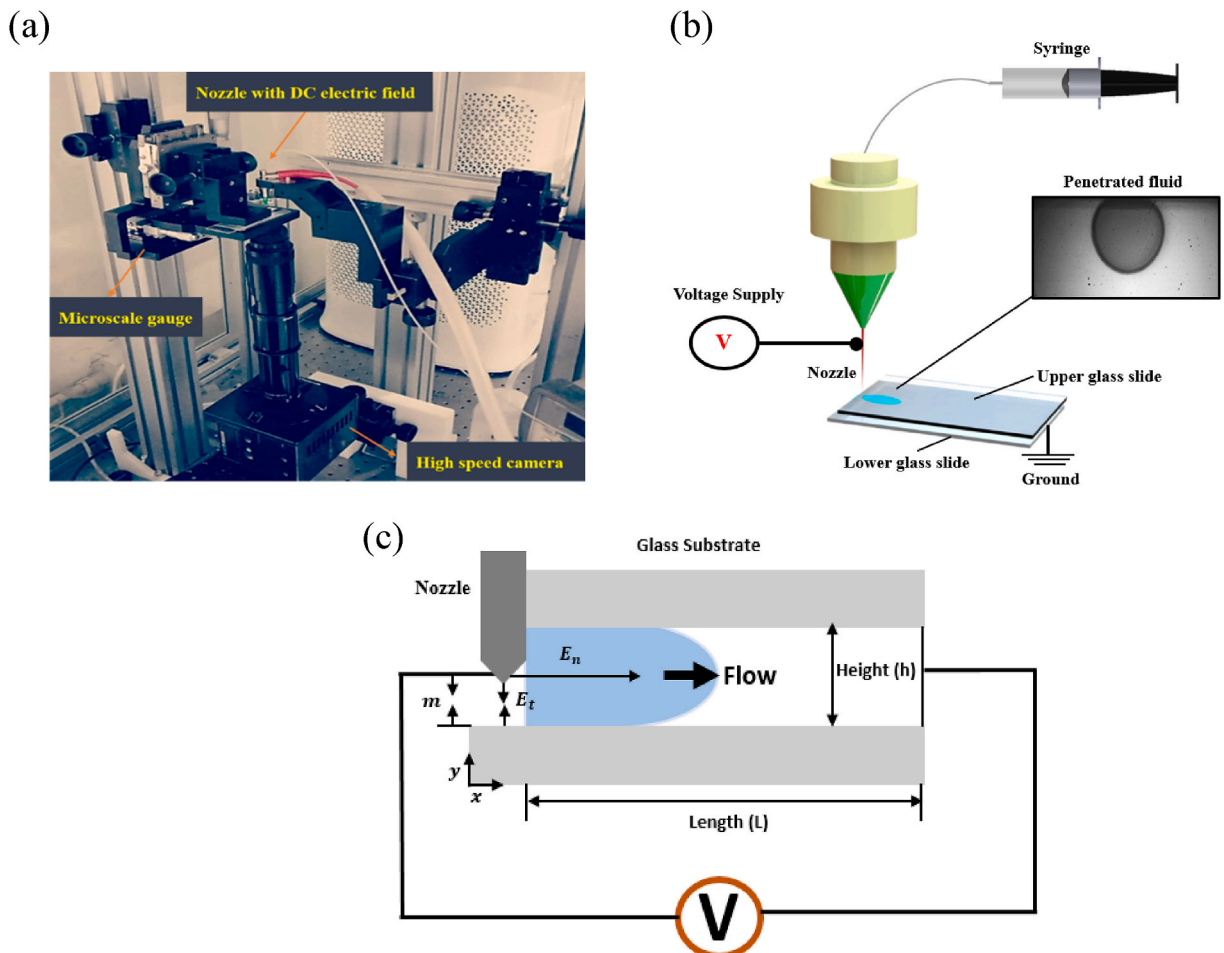

Fig. 1. Schematic of the experimental setup, and fluid flow between parallel plates under the effect of electric potential. (**a**) experimental setup with a high-speed camera and electric field generation; (**b**) experimental setup; a voltage is applied to the nozzle near the meniscus between the parallel plates; (**c**) voltage effect on the fluid flow between parallel plates with channel height h and length L. Different viscous fluids were pumped using a syringe pump and nozzle under a high voltage.

Table 1
Experimental parameters and conditions.

Experimental parameters	
Substrate	Glass
Length of channel	0.004 m
Flow rate (Q)	5.33×10^{-11} m^3/s
Nozzle outer diameter (D)	0.000250 m
Slit gap	100 μm
Nozzle height from the substrate (m)	50 μm
Voltages	0–500 V

3. Numerical simulation

A three-dimensional (3D) numerical simulation analysis was performed to analyze and endorse experimental results of an external electric field effect on the capillary-driven flow between parallel plates. COMSOL Multiphysics software was used to perform a time-dependent simulation that included a quasi-electrostatic module, a level set module, and a laminar two-phase flow. The effect of an increase in the applied electric field on capillary-driven flow was evaluated to confirm the experimental findings of this study. The electrostatic interface, the laminar two-phase flow, and the level-set module were configured separately. The physics coupling was performed using Maxwell electrical stress tensors between electrostatic forces and laminar flow. Maxwell stress tensor is a method generally used to compute the volume force acting on a system. Similar to that in the experiment, the contact angle (15.4°) for the glass surface was set based on the condition of the wetted-wall boundary on the inner sides of the parallel plates (Fig. S1). The slip length was set to default as a factor of minimum element length and, parametrically varied from 0 to 1.5 while keeping the minimum mesh element length of 4 μm at the wall. The factor was set to be 0.75 as it yielded results with quite low residual error and a smaller value for slip length would force the mesh to be more refined, increasing the overall computational time.

The Navier–Stokes equation was used to determine the fluid motion between air and fluid. As the theoretical and experimental outcomes required a mean interface location, a basic interface tracking model was performed using the level-set method. The changing permittivity gradient and conductivity between the fluids caused the appearance of charge and thus, a localized electric force at the interface [54]. The electric force acting on the fluid due to the development of surface charges at the interfaces was examined using local electric fields. The divergence of the Maxwell electric tensor can be used to acquire the electrostatic body force density; this body force, which expresses the electrostatic force produced by a non-uniform electric field, was represented as an external force within the Navier–Stokes equation, which was used to create the numerical coupling (Equations (5) and (6)). The components required for computing the Maxwell tensor divergence are the electric field and the dynamic permittivity of each mesh element based on the volume ratio of fluid/air in that element. These parameters were derived from the electrostatic module, and force components were calculated accordingly in Equation (9) for each mesh node. The derived force acts on the entire system; therefore, it was added as a volume force (F) in the laminar two-phase flow module (Equation (1)); hence the coupling between both modules was achieved. To further understand, we represented the multi-physics setup for the laminar two-phase flow; a level-set interface module was used to set up the equations for the fluid motion according to the Navier-Stokes equation [55]:

$$\rho \frac{\partial u}{\partial t} + \rho (u \cdot \nabla)u = \nabla \cdot \left[-pI + \mu \left(\nabla u + (\nabla u)^T \right) \right] + F_{st} + \rho g + F \tag{1}$$

$$\nabla \cdot u = 0 \tag{2}$$

Where u, , μ, p and g denote the velocity, density, dynamic viscosity, pressure, and gravity, respectively (Equation (2)). F_{st} is the surface tension force, I is the identity matrix, and F is the additional volume force, i.e., electrical force. To track the fluid interface, the level set equation was described as follows [55]:

$$\frac{\partial \varnothing}{\partial t} + u \cdot \nabla \varnothing = \alpha \nabla \cdot \left(\in_{ls} \nabla \varnothing - \varnothing (1 - \varnothing) \frac{\nabla \varnothing}{|\nabla \varnothing|} \right) \varnothing \tag{3}$$

In above Equation (3), α controls the reinitialization (m/s), $\in_{ls}$ denotes the interface thickness and $\varnothing$ is the level set variable. The electrostatics interface module set up the following equation for the electric potential V:

$$-\nabla \cdot (\varepsilon_0 \varepsilon_r \nabla V) = 0 \tag{4}$$

Here in Equation (4), ε_0 is the permittivity of vacuum, and ε_r is the dynamic permittivity of the fluid domain which is dependent on the fluid fraction of both liquids. Finally, physics coupling was performed by adding the Maxwell electrical stress to the Navier-Stokes equation to include the external electric field force acting on the system. This external electric field force, induced by the divergence of Maxwell stress tensor, is mathematically expressed as;

$$F = \nabla \cdot T \tag{5}$$

$$T = ED^T - I \tag{6}$$

where T denotes the Maxwell stress tensor, E is the electric field, D is the electric displacement field the superscript T denotes the transpose operator while I is the identity matrix. The expanded form of the stress tensor shown in Equation (6) is as following [56] (Equations (7) and (8)):

$$E = -\nabla V \qquad (7)$$

$$D = \varepsilon_0 \varepsilon_r E \qquad (8)$$

$$T = \begin{bmatrix} T_{xx} & T_{xy} & T_{xz} \\ T_{yx} & T_{yy} & T_{yz} \\ T_{zx} & T_{zy} & T_{zz} \end{bmatrix} = \begin{bmatrix} \varepsilon_0 \varepsilon_r E_x^2 - \frac{1}{2}\varepsilon_0 \varepsilon_r \left(E_x^2 + E_y^2 + E_z^2 \right) & \varepsilon_0 \varepsilon_r E_x E_y & \varepsilon_0 \varepsilon_r E_x E_z \\ \varepsilon_0 \varepsilon_r E_y E_x & \varepsilon_0 \varepsilon_r E_y^2 - \frac{1}{2}\varepsilon_0 \varepsilon_r \left(E_x^2 + E_y^2 + E_z^2 \right) & \varepsilon_0 \varepsilon_r E_y E_z \\ \varepsilon_0 \varepsilon_r E_z E_x & \varepsilon_0 \varepsilon_r E_z E_y & \varepsilon_0 \varepsilon_r E_z^2 - \frac{1}{2}\varepsilon_0 \varepsilon_r \left(E_x^2 + E_y^2 + E_z^2 \right) \end{bmatrix} \qquad (9)$$

Finally, the divergence of the tensor, as mentioned above (Equation (9)), was added to the Navier-Stokes equation (1) for coupling the Multiphysics simulation setup. The simulation geometry was built using the experimental setup as a guide. The applied conditions, including the flow rate (5.33×10^{-11} m³/s), electrode position and voltage variation (0 and 500 V) were the same as those used in the tests. The outlet boundary condition was set to 0 Pa, and the ground boundary condition was placed at the outlet. Based on the potential applied, the electric field components E_x, E_y and E_z were determined locally as the fluid interface changed with time. Finally, the electrical force calculated by COMSOL in the quasi-electrostatic simulation was connected to the fluid dynamics simulation to provide a realistic simulation of the phenomenon. As a result, when the applied voltage was increased, the Maxwell stress produced by the voltage at the fluid interface dominantly influenced the fluid flow penetration length.

A 3D rectangular micro-channel was designed with a slit gap of 100 μm, length of 4 mm, and width of 2 mm, as shown in Fig. 2a; a circular microchannel was also constructed, depicting the flow path as the inlet of a rectangular microchannel. This circular microchannel diameter was 250 μm, the same as the syringe outer diameter, while the length was set to be 50 μm depicting the syringe to slit distance (m). The boundary conditions for the simulation were set to be equivalent to our experimental setup. The system inlet/syringe outlet was specified to have a constant flow rate of 5.33×10^{-11} m³/s. The side walls were given a no-flow condition while the
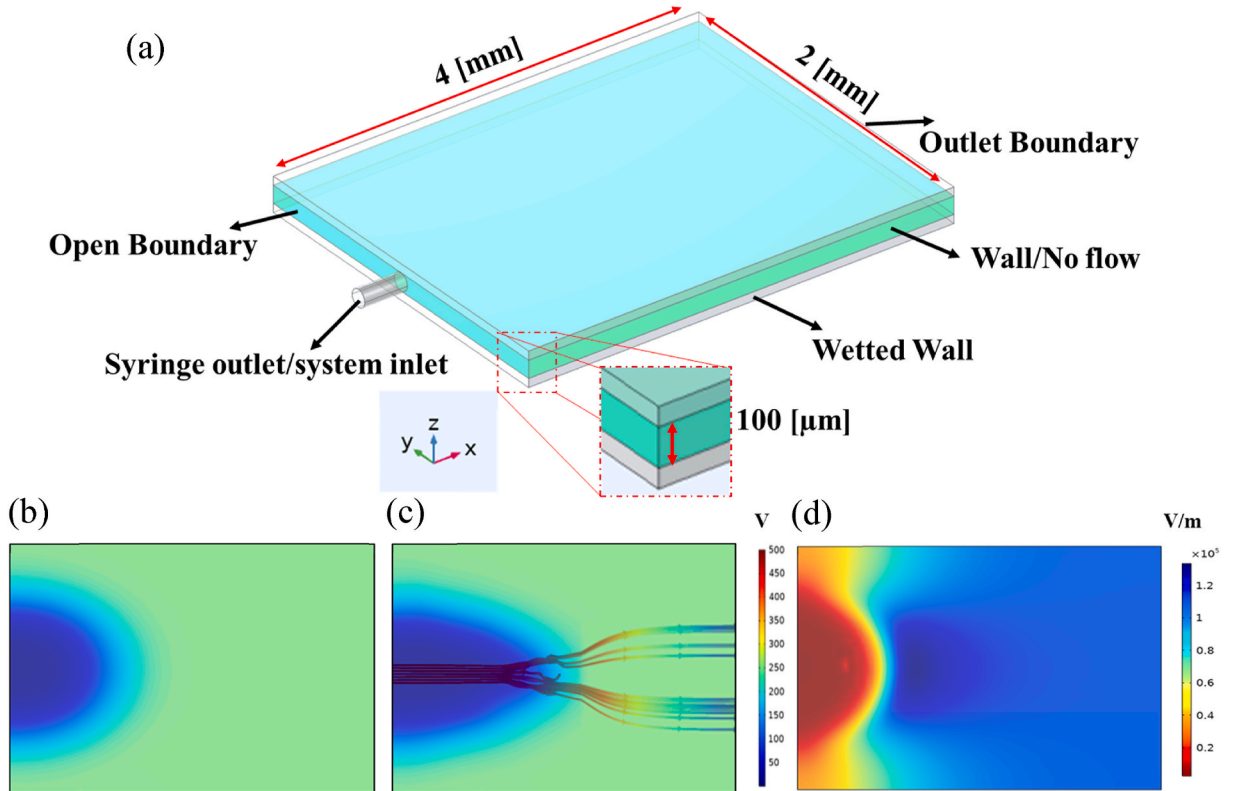

Fig. 2. Comparison of numerical simulation results for meniscus flow at 0 and 500 V. (**a**) schematic of channel and boundary conditions; (**b**) volume fraction of the fluid flow at 0 V under the capillary effect; (**c**) volume fraction of the fluid flow with the electric field streamline (V) at 500 V; (**d**) representation of electric field norm (V/m) and pressure contour of the fluid flow at 500 V.

outlet boundary was set at 0 gauge or static atmospheric pressure. The up and down walls were given the wetted wall boundary condition. Fig. 2b and c shows the comparison of fluid flow at 0 and 500 V, where the contour plot in Fig. 2d represents electric field norm variations across the system, which indicates a higher intensity of the electric field norm (V/m) owing to the higher permittivity and polar conductivity of the field compared with the corresponding values for air. The contour lines indicate the pressure (Pa) from the inlet to the channel outlet. Within the fluid domain, the colour of the streamline represents a change in the applied voltage, whereas the streamline density indicates the electric field intensity. It is known that electric field lines tend to pass through high-permittivity media. The simulation defined the electric permittivity as the proportionality factor between the electrical polarization and field strength. The proportionality factor was dynamically computed according to the changing volume fraction in the mesh element of the defined domain. The proportionality factor is computed in each mesh element from the internally defined volume fractions of each fluid for the relative permittivity of air and liquid, respectively. A numerical simulation study was performed to analyze the effect of a non-uniform electric field on a liquid owing to the variation of the permittivities. The advancing fluid front was also observed, revealing the influence of an applied electric field on the penetration length, thus confirming the experimental results.

4. Results and discussion

4.1. Capillary number

The viscous to surface tension force ratio $\left(\frac{\mu u}{\gamma}\right)$ [57,58] is known as the capillary number (C_a). Here, u represents the flow velocity of the fluid. Typically, the flow between parallel plates is dominated by capillary forces at low C_a ($C_a \leq 1$), and viscous forces are dominant at high C_a ($C_a \geq 1$). As illustrated in Fig. S2a, C_a increases when the viscosity of the fluid increases at 0 V, indicating substantial viscous effects on the fluid flow. Similarly, C_a also increases continuously as the fluid flow advances between the parallel plates, indicating the dominance of viscous forces over surface tension forces. In our analysis, the capillary number values were not high, hence our experiments were dominated by capillary forces over viscous forces. Therefore, C_a plays an important role in analyzing the effects of viscosity on the underfill fluid flow length. In this study, the electric field and polarity effects were analyzed further to overcome the slower speed of highly viscous fluids.

4.2. Electrocapillary number

Electric forces play a vital role in fluid flow dynamics when a voltage is applied between the meniscus and the ground on the other side of the parallel plates. To examine the effect of external electric forces on the fluid flow length, the electrocapillary number (C_{a_E}) is analyzed, where C_{a_E} is defined as the ratio of the electric forces to the surface tension forces, as follows [59–61].

$$C_{a_E} = \left(\frac{\varepsilon_m E^2 h}{\gamma}\right),$$
(10)

where $h, E,$ and ε_m represent the distance between the parallel plates, electric field, and permittivity, respectively. The impact of C_{a_E} on the fluid flow is depicted in Fig. S2b for EG, where an increase in the electrocapillary number improves the fluid flow length owing to the high electric field and strong polarity effects. Without an external pressure gradient, the EHD pumps require either a permittivity gradient across the field or a weakly conducting incompressible dielectric fluid that can only be made to flow in the presence of an electric field if space charges are generated in the fluid. The electric field created by the EHD flow can be used to achieve the bulk flow driven by the Maxwell electric pressure gradient [62], which may arise without interfacial charges, owing to the gradient in the normal component of the Maxwell stress tensor. Because we wished to investigate the capillary flow penetration length between the plates, we modeled the fluid flow length (L) in the x-direction (Fig. 1b) under tangential and normal electric forces. A normal force is applied along the channel length tangentially to the plate direction. A voltage source also generates an electric field at the nozzle end, which acts as an electrode near the parallel plates meniscus, driving a fluid flow similar to that of the EHD phenomenon [63]. Electric force induces not only motion but polarization; thus, the flow perturbs by the electric field and therefore alters the flow length.

4.3. Effect of liquid viscosity on capillary flow

In this section, we present a substantial dataset that characterizes the dynamics of the flow length versus time for various viscous liquids in the absence of an electric field. The contact line expands when the fluid touches the inlet of the parallel plates, and the capillary force causes the liquid to flow along the parallel plates. The capillary-driven flow time can be calculated using the Washburn equation, as follows [64–67]:

$$t = \frac{3\mu l(t)^2}{h\gamma \cos\theta}$$
(11)

where $l(t), \mu, \gamma, \theta,$ and h denote the instantaneous penetration distance of the liquid, viscosity, surface tension, contact angle, and the gap between parallel plates, respectively. Fig. 3a illustrates the effect of viscosity on the capillary-driven fluid flow of various viscous fluids (0.0018–1.2 Pa. s), including 30% methanol in DI (MD), 20% ethanol in DI (ED), 50% ethylene glycol in DI (EGD), 50% glycerol in DI (GD), and pure glycerol (G) at 0 V for 0.1–1.2 s. The underfill fluid flow length of MD reached a maximum of approximately 0.78

mm at 0.1 s, where the flow length of the low viscosity liquid (MD) near the meniscus was higher than that of EGD (0.58 mm) and GD (0.45 mm) in the same time interval. The fluid flow lengths of MD and pure glycerol at 1.2 s were 2.51 and 1.13 mm, respectively; a 54% decline in the flow length of the pure glycerol fluid was observed compared with that in the low viscosity liquid MD. These results indicate viscosity is the most important factor influencing the underfill fluid flow length. The meniscus location was dependent on the viscosity of the fluid and the meniscus of highly viscous fluid was shorter than that of a low viscosity fluid at the same time interval owing to highly viscous forces. Equation (11) indicates that an increase in the viscosity [68] increases the filling time of the underfill fluid, which accurately reflects our experimental evaluations. Thus, we can conclude that an increase in the viscosity of a fluid
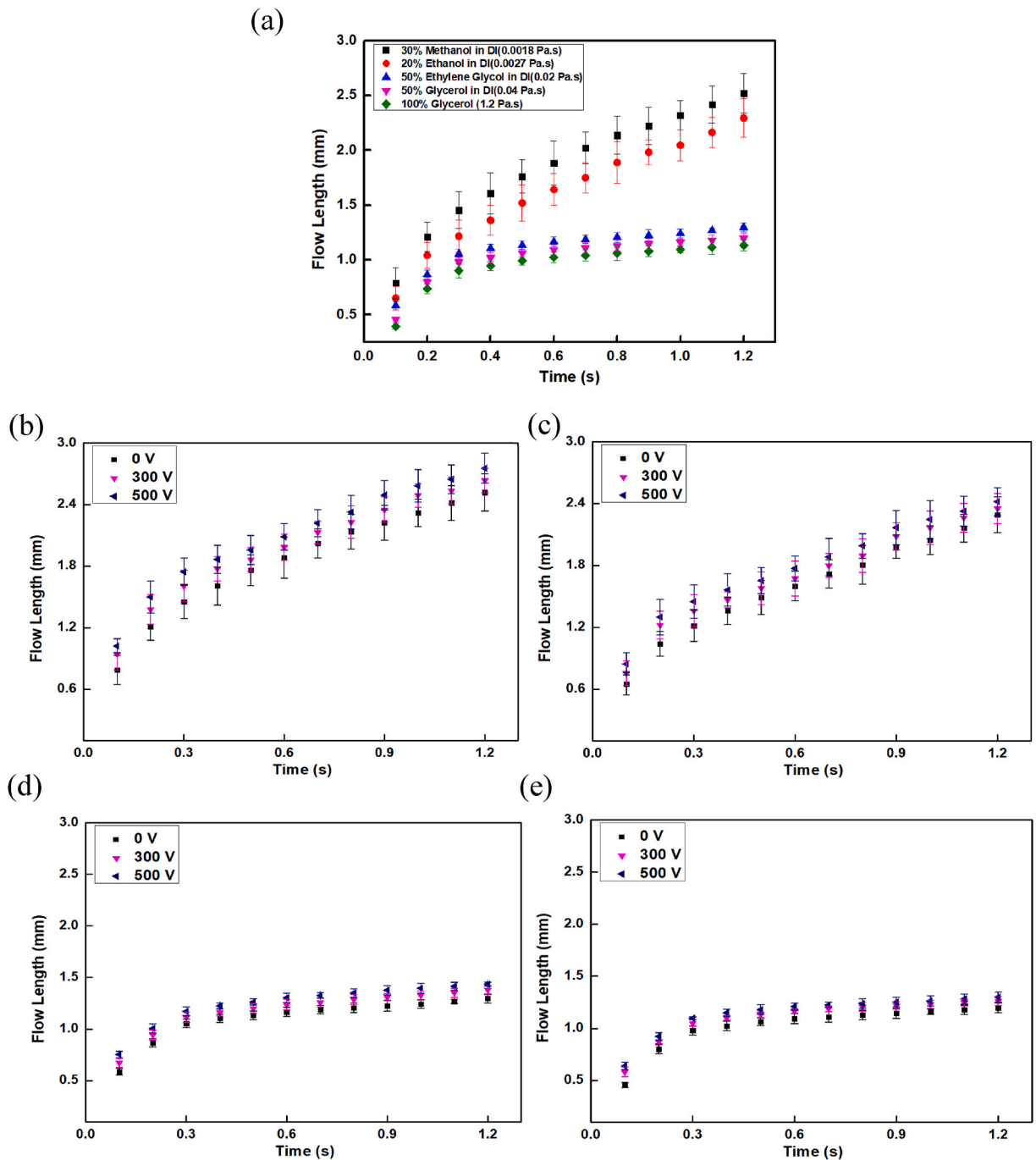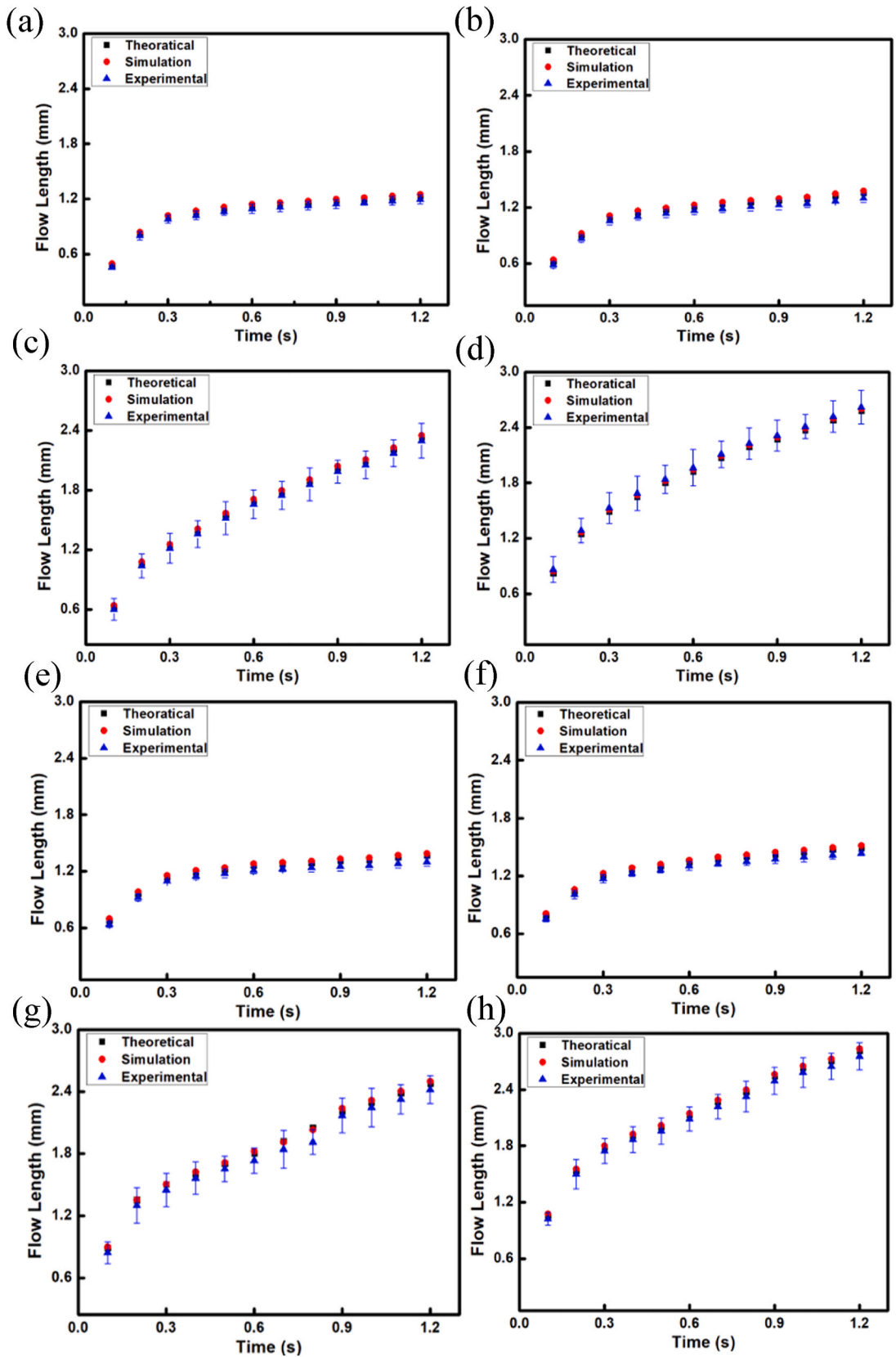

Fig. 3. Electric field effect on the penetration flow length of different viscous fluids (a) comparison of the penetration lengths of the different viscous fluids at 0 V (**b**) 30% methanol in DI water; (**c**) 20% ethanol in DI water; (**d**) 50% ethylene glycol in DI water; and (**e**) 50% glycerol in DI water.

(caption on next page)

Fig. 4. Comparison of theoretical, numerical, and experimental results for different viscous fluid penetration flow lengths under an electric field. (a, b, c, and d) penetration flow length of 50% glycerin in DI water, ethylene glycol in DI water, 20% ethanol in DI water, and 30% methanol in DI water at 0 V. **(e, f, g, and h)** penetration flow length of 50% glycerin in DI water, 50% ethylene glycol in DI water, 20% ethanol in DI water, and 30% methanol in DI water at 500 V.

increases the underfill flow time, which is the primary drawback of the underfill technology.

4.4. Effect of electric field on viscous fluid flow

The influence of the electrical potential on the spreading behaviour of several viscous fluids (MD, ED, EGD, and GD) was investigated while maintaining a similar surface tension value (27–34 mN/m) for all the working fluids. Certain combinations of liquids were found in literature [69–71], for which different concentrations of the different liquids had a similar surface tension; this was also verified experimentally. An electrical potential was applied to the nozzle near the meniscus formed between the parallel plates to reduce the filling time of the viscous fluids. The flow-length patterns observed at various voltages are illustrated in Fig. 3(c, d, and e). The low viscous fluids are exponential in the range of 0.1–1.2 s, as shown in Fig. 3b and c, whereas the equilibrium position of the high viscous fluids was achieved at 1.2 s, as depicted in Fig. 3(d and e). Therefore, we selected the range from 0.1 to 1.2 s for all liquids in our measurements. At 0 V, the fluid profile widens as the fluid pierces through the gap between the parallel plates, demonstrating the capillary effect for all the working fluids. At 500 V and 1.2 s, the MD, ED, EGD, and GD liquids exhibit maximum fluid flow penetration lengths of 2.75, 2.42, 1.43, and 1.29 mm, respectively (Fig. 3(b, c, d, and e)). Results show that the low viscosity fluid MD demonstrates a more significant fluid flow penetration length (2.75 mm), which is substantially higher compared to that of a highly viscous fluid, such as GD (1.29 mm). These results indicate that the flow length increases gradually with an increase in the electrical potential for all working fluids. The induced electrical potential increases the flow length of the highly viscous fluids, thereby overcoming partial and slow underfilling. In summary, our findings indicate that an increased fluid flow penetration length is associated with the capillary number, viscous fluid, and a high electrocapillary number.

4.5. Comparison between theoretical, numerical, and experimental results

Fig. 4 shows a comparison of the experimental and numerical simulation results with the theoretical model [19] for different viscous fluids at different voltages (0 and 500 V). The experimentally observed values of the viscosity, surface tension, voltages, nozzle height from the substrate, and length of parallel plates are presented in Tables 1 and 2 and employed in the comparison of the experimental results with those of the numerical simulation and theoretical model. The fluid flow penetration length is a function of the following three driving forces: electric, inlet, and capillary pressures. The theoretical model used simulated and average experimental data from several time steps to examine the meniscus location and flow of the different viscous fluids. Fig. 4 (a, b, c, and d) shows a comparison of penetration flow length of 50% glycerin in DI water, ethylene glycol in DI water, 20% ethanol in DI water, and 30% methanol in DI water at 0 V respectively. Fig. 4 (e, f, g, and h) represents the effect of voltage to enhance the penetration flow length of different viscous fluids at 500 V. This comparison was used to determine the fluid flow length until it reaches the gap, along with the distribution profile between parallel plates. Upon comparing the experimental data with that of the simulation and theoretical models, we discovered that all experimental results exhibited an average variance of 4–7%. Consequently, these findings can be considered proof of the enhancement in the fluid flow penetration length resulting from the externally applied electric field.

4.6. Effect of polarity on the fluid flow

The voltage has a higher impact on the low viscous fluids than the high viscous fluids due to the low viscous forces. As shown in Fig. 3, when the viscosity of a fluid is increased, the effect of voltage decreases; therefore, further experiments were performed by adding conductive NaCl in viscous glycerin fluid. The effect of ionic concentrations under an electric field was examined to address the slow filling of the highly viscous fluid. NaCl was mixed with glycerin to elucidate the effect of fluid polarity on the underfill fluid flow length under the effect of an electric field. A maximum of 4 wt% NaCl completely dissolved in the glycerin with the highest polarity

Table 2
Viscosity, surface tension, and conductivity of different viscous fluids (with and without NaCl).

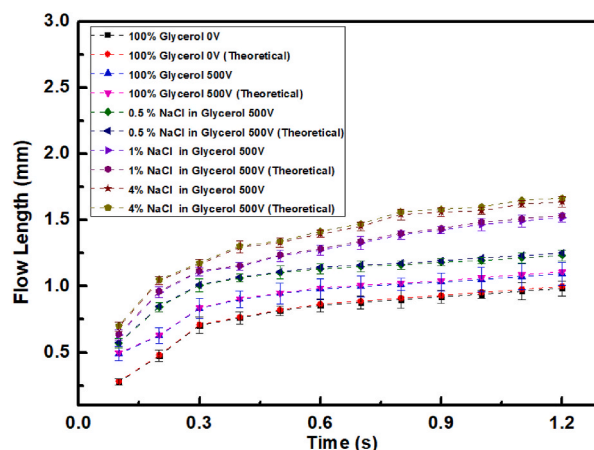| Liquids	Viscosity (Pa.s)	Surface Tension (mN/m)	Conductivity (μS/cm)
30% Methanol/DI	0.0018	32	5.76
20% Ethanol/DI	0.0022	34	5.05
50% Ethylene Glycol/DI	0.02	27	2.47
50% Glycerol/DI	0.04	30	8.94
100% Glycerol	1.20	63.4	2
0.1% NaCl/glycerol	1.25	8.30	30
0.5% NaCl/glycerol	1.31	8.10	70
1% NaCl/glycerol	1.38	7.54	135
2% NaCl/glycerol	1.45	7.20	154
4% NaCl/glycerol	1.52	6.80	195

Fig. 5. Comparison of theoretical and experimental results of the electric field effect on the penetration flow length of glycerol and NaCl/glycerol at varying concentrations of NaCl; viscosities ranging from 1.2 to 1.52 Pa s.

(Fig. S3), whereas higher quantities (6% and 8%) resulted in agglomeration in the solution. A comparison between the effects of the electric field and fluid polarity at varying glycerol and NaCl/glycerol concentrations is shown in Fig. 5; herein, a similar pattern of fluid flow is observed in the case of all curves, which illustrates that at the initial level, the flow drastically increases, and the gradually decreasing behaviour of the fluid flow can be attributed to air and frictional forces. Glycerol (NaCl = 0) demonstrated the lowest viscosity among all tested NaCl/glycerol solutions and spread slowly approximately up to 0.98 mm at 1.2 s; the flow length of glycerol (NaCl = 0) increased only by 12%, despite the application of an electric potential of 500 V. Fig. 5 shows that NaCl/glycerol responded effectively in fluid flow length under electric field influence due to improved conductivity of NaCl/glycerol concentrations; however, the viscosity increased, and surface tension decreased by adding NaCl in glycerol (Table 2). Therefore, in our measurements, conductivity has a dominating role in enhancing fluid flow length under the electric field effect. Increased concentrations of NaCl/glycerol resulted in longer underfill flow lengths between the parallel plates owing to the high polarity interaction between the solution and electric potential difference. The electrical polarization of a substance is determined based on its permittivity, which is directly proportional to C_{a_E} in the electrocapillary number equation (Equation (10)). A higher electrocapillary number indicates a highly polarized fluid in the system (Fig. S4). Based on this, we can conclude that the stronger the polarity effect within a substance, the higher is the permittivity of the system and, hence, the higher is the electrocapillary number. Owing to the strong polarity and higher system permittivity gradient across the substance, the underfill flow length improved when the electrocapillary number increased. Compared with glycerol at 0 V, the presence of 4% NaCl in glycerol increased the penetration length of the highly viscous fluid flow by 41% under an applied electric potential of 500 V. The fluid flow length of glycerol increased from 0.98 mm (glycerol alone) to 1.22 and 1.55 mm upon adding 0.5% and 1% concentrations of NaCl respectively at 1.2 s. This represents a significant improvement of about 20% and 37%, respectively, in the flow length and shows how even a small amount of additive can increase the flow length of viscous conductive fluids. Fig. 5 also presents a comparison of the experimental and theoretical results obtained when NaCl is added to high-viscosity glycerol. We observed the effect of voltage increased the fluid flow length of NaCl/glycerol liquid by overcoming the viscous forces due to enhanced conductance of NaCl/glycerol liquid. The permittivity of fluid also plays an important role in the electric field effect, which can be further studied.

5. Conclusion

It is known that the viscosity of a fluid considerably affects the dynamics of capillary-driven flow in microfluidic devices and underfill applications. In research and industrial operations, high-viscosity fluids increase the viscous resistance, thereby decelerating the penetration flow length, which is undesirable. With the electronic industry moving toward more efficient chip packaging processes in terms of underfilling and functionality, the rapidly flowing of highly viscous fluids is becoming increasingly important.

Herein, we investigated the effect of viscosity on underfill fluid flow length with respect to C_a, C_{a_E}, polarity, and electric field effects. Consequently, we noticed that the increment in C_a owing to high viscosity reflected the presence of substantial viscous effects in the viscous fluid flow. In the case of electrocapillary number, an increment in C_{a_E} lead to an increased underfill fluid flow length due to the enhanced electric field and permittivity effects. Furthermore, the effects of the electric field on highly viscous fluids were examined; owing to the applied electrical potential, the penetration flow length of the viscous fluids increased by 45% compared to that under capillary-driven flow without the electric field effect. The effect of the electric field on low-viscosity fluids was found to be prominent compared to that on high-viscosity fluids, owing to increased viscous forces. To overcome the effect of the viscous force, we modified the fluid polarity by adding NaCl to glycerol, and the results indicated a longer underfill flow length than that for glycerol under the effect of an electric field. We further discovered that compared to glycerol at 0 V, 4% NaCl in glycerol under an applied electrical potential of 500 V increased the penetration length of the highly viscous fluid flow by 41%. In particular, adding 0.5% NaCl to glycerol increased the underfill flow length by 20%, demonstrating that even a small amount of additive, could significantly increase

the flow length under the electric potential effect by enhancing the polarity of the fluid.

The research presented here can have implications in point-of-care diagnostic equipment, viscous and conductive liquids mixing, and transportation of highly viscous oils and organic solvents, where working fluids demonstrate a wide variety of properties. In the future, highly viscous fluids can be studied to analyze flow characteristics under electric field effects. More conductive particles/ materials can be embedded in highly viscous materials to study their characteristics under electric field effects. The experimental and simulation-based study can be investigated to analyze the shear thinning viscosity behavior and dynamics of non-Newtonian fluid flow under the electric field and thermal effects.

Author contribution statement

Rizwan Ul Hassan: Conceived and designed the experiments; Performed the experiments; Analyzed and interpreted the data; Contributed reagents, materials, analysis tools or data; Wrote the paper.

Shaheer Mohiuddin Khalil, Joonkyeong Moon: Contributed reagents, materials, analysis tools or data.

Saeed Ahmed Khan, DaeHyun Cho, Doyoung Byun: Analyzed and interpreted the data.

Data availability statement

Data will be made available on request.

Declaration of competing interest

The authors declare that they have no known competing financial interests or personal relationships that could have appeared to influence the work reported in this paper.

Acknowledgment

Appendix A. Supplementary data

Supplementary data to this article can be found online at https://doi.org/10.1016/j.heliyon.2023.e16395.

References

[1] V.M. Kulkarni, K.N. Seetharamu, I. Abdul Azid, P.A. Aswatha Narayana, G. Abdul Quadir, Numerical simulation of underfill encapsulation process based on characteristic split method, Int. J. Numer. Methods Eng. 66 (10) (2006) 1658–1671, https://doi.org/10.1002/nme.1704.

[2] C.Y. Khor, M.Z. Abdullah, Z.M. Ariff, W.C. Leong, Effect of stacking chips and inlet positions on void formation in the encapsulation of 3D stacked flip-chip package, Int. Commun. Heat Mass Tran. 39 (5) (2012) 670–680, https://doi.org/10.1016/j.icheatmasstransfer.2012.03.023.

[3] P.C. Li, E.J. Cotts, Y. Guo, G.L. Lehmann, Viscosity measurements and models of underfill mixtures, Proc. 3rd Int. Conf. Adhes. Join. Coat. Technol. Electron. Manuf. (1998) 328–333, https://doi.org/10.1109/ADHES.1998.742049. ADHES 1998 1998, 1998-Septe.

[4] H. Wang, H. Zhou, Y. Zhang, D. Li, K. Xu, Three-dimensional simulation of underfill process in flip-chip encapsulation, Comput. Fluids 44 (1) (2011) 187–201, https://doi.org/10.1016/j.compfluid.2010.12.030.

[5] Y. Guo, G.L. Lehmann, T. Driscoll, E.J. Cotts, Model of the underfill flow process: particle distribution effects, Electron. Compon. Technol. Conf. (1999) 71–76, https://doi.org/10.1109/ectc.1999.776066.

[6] K. Wang, Y. Wang, W. Zhu, Prediction of filling time in capillary-driven underfill process through 3D numerical analysis, 19th Int. Conf. Therm. Mech. Multi-Physics Simul. Exp. Microelectron. Microsystems, EuroSimE (2018) 1–5, https://doi.org/10.1109/EuroSimE.2018.8369911, 2018 2018.

[7] R. Straessle, S. Zimmermann, L. Carro, S. Member, J. Zürcher, S. Member, G. Schlottig, A. Achen, G. Hong, D. Poulikakos, T. Brunschwiler, S. Member, Percolating microparticles applied as underfill, IEEE Trans. Compon. Packag. Technol. 8 (5) (2018) 840–850.

[8] Y.J. Wan, G. Li, Y.M. Yao, X.L. Zeng, P.L. Zhu, R. Sun, Recent advances in polymer-based electronic packaging materials, Compos. Commun. 19 (2020) 154–167, https://doi.org/10.1016/j.coco.2020.03.011.

[9] C.Y. Huang, L.C. Shen, T.H. Wu, C. Greene, Application of multi-quality parameter design in the optimization of underfilling process – a case study of a vehicle electronic module, Solder. Surf. Mt. Technol. 33 (2) (2021) 128–138, https://doi.org/10.1108/SSMT-05-2020-0016.

[10] Y. Li, C. Zhong, C. Li, R. Jiang, J. Lu, R. Sun, Mold Flow Simulation Analysis of Molded Underfill in an Ultra-thin High-Density Package, 2022, pp. 84–89.

[11] S. Huang, J. Song, Y. Lu, F. Chen, H. Zheng, X. Yang, X. Liu, J. Sun, C.J. Carmalt, I.P. Parkin, W. Xu, Underwater spontaneous pumpless transportation of nonpolar organic liquids on extreme wettability patterns, ACS Appl. Mater. Interfaces 8 (5) (2016) 2942–2949, https://doi.org/10.1021/acsami.5b08596.

[12] H. Wang, Y. Su, W. Wang, G. Sheng, H. Li, A. Zafar, Enhanced water flow and apparent viscosity model considering wettability and shape effects, Fuel 253 (2019) 1351–1360, https://doi.org/10.1016/j.fuel.2019.05.098.

[13] M.S. Mahmud, A. Alo, B. Farshchian, G.H. Lee, N. Kim, Pulsed laser ablation on polymethylmethacrylate (PMMA) surfaces for capillary driven flows, Surface. Interfac. 31 (2022), https://doi.org/10.1016/j.surfin.2022.101989.

[14] K. Keshmiri, H. Huang, A.B. Jemere, N. Nazemifard, Investigation of capillary filling dynamics of multicomponent fluids in straight and periodically constricted microchannels, Langmuir 36 (22) (2020) 6304–6313, https://doi.org/10.1021/acs.langmuir.0c00128.

[15] I. Jang, H. Kang, S. Song, D.S. Dandy, B.J. Geiss, C.S. Henry, Flow control in a laminate capillary-driven microfluidic device, Analyst 146 (6) (2021) 1932–1939, https://doi.org/10.1039/d0an02279a.

[16] G. Nagayama, S. Gyotoku, T. Tsuruta, Thermal performance of flat micro heat pipe with converging microchannels, Int. J. Heat Mass Tran. 122 (2018) 375–382, https://doi.org/10.1016/j.ijheatmasstransfer.2018.01.131.

[17] X. Xie, Q. Weng, Z. Luo, J. Long, X. Wei, Thermal performance of the flat micro-heat pipe with the wettability gradient surface by laser fabrication, Int. J. Heat Mass Tran. 125 (2018) 658–669, https://doi.org/10.1016/j.ijheatmasstransfer.2018.04.110.

[18] R. Fu, H. Zhang, X. Hu, Y. Yan, W. Zhou, Effect of the hotter groove on the capillary flow enhancement with nanofluids in a microgrooves wick, Int. Commun. Heat Mass Tran. 127 (2021), 105512, https://doi.org/10.1016/j.icheatmasstransfer.2021.105512.

[19] R. Ul Hassan, J. Lee, S.M. Khalil, G. Kang, D.H. Cho, D. Byun, Experimental, theoretical, and numerical investigation of the electric field and surface wettability effects on the penetration length in capillary flow, ACS Omega 6 (48) (2021) 32773–32782, https://doi.org/10.1021/acsomega.1c04629.

[20] N.K. Karna, A. Rojano Crisson, E. Wagemann, J.H. Walther, H.A. Zambrano, Effect of an external electric field on capillary filling of water in hydrophilic silica nanochannels, Phys. Chem. Chem. Phys. 20 (27) (2018) 18262–18270, https://doi.org/10.1039/c8cp03186j.

[21] X. Liu, G. Hao, B. Li, Y. Chen, Experimental study on the electrohydrodynamic deformation of droplets in a combined DC electric field and shear flow field, Fundam. Res. (2022), https://doi.org/10.1016/j.fmre.2021.10.011.

[22] B. Mahapatra, A. Bandopadhyay, Numerical analysis of combined electroosmotic-pressure driven flow of a viscoelastic fluid over high zeta potential modulated surfaces, Phys. Fluids 33 (1) (2021), https://doi.org/10.1063/5.0033088.

[23] A. Steinberger, C. Cottin-Bizonne, P. Kleimann, E. Charlaix, High friction on a bubble mattress, Nat. Mater. 6 (9) (2007) 665–668, https://doi.org/10.1038/nmat1962.

[24] R. Blossey, C. Scientifique, Self-Cleaning Surfaces — Virtual Realities, 2003, pp. 301–306.

[25] J.P. Rothstein, Slip on superhydrophobic surfaces, Annu. Rev. Fluid Mech. 42 (2010) 89–109, https://doi.org/10.1146/annurev-fluid-121108-145558.

[26] U. en, S. Chatterjee, R. Ganguly, R. Dodge, L. Yu, C.M. Megaridis, Scaling laws in directional spreading of droplets on wettability-confined diverging tracks, Langmuir 34 (5) (2018) 1899–1907, https://doi.org/10.1021/acs.langmuir.7b03896.

[27] A. Abas, M.H.H. Ishak, M.Z. Abdullah, Finite volume analysis of pressurized underfill encapsulation process, ARPN J. Eng. Appl. Sci. 11 (1) (2016) 166–171.

[28] Z.L. Gan, A. Abas, M.H.H. Ishak, M.Z. Abdullah, J.L. Ngang, Comparative study of pressurized and capillary underfill flow using lattice Boltzmann method, Arabian J. Sci. Eng. 44 (9) (2019) 7627–7652, https://doi.org/10.1007/s13369-019-03866-y.

[29] T.G. Myers, J.P.F. Charpin, M.S. Tshehla, The flow of a variable viscosity fluid between parallel plates with shear heating, Appl. Math. Model. 30 (9) (2006) 799–815, https://doi.org/10.1016/j.apm.2005.05.013.

[30] W. Bin Young, W.L. Yang, Underfill viscous flow between parallel plates and solder bumps, IEEE Trans. Compon. Packag. Technol. 25 (4) (2002) 695–700, https://doi.org/10.1109/TCAPT.2002.806176.

[31] T.S. Sammarco, M.A. Burns, Thermocapillary pumping of discrete drops in microfabricated analysis devices, AIChE J. 45 (2) (1999) 350–366, https://doi.org/10.1002/aic.690450215.

[32] S. Daniel, M.K. Chaudhury, J.C. Chen, Fast drop movements resulting from the phase change on a gradient surface, Science 291 (5504) (2001) 633–636, https://doi.org/10.1126/science.291.5504.633.

[33] A.A. Darhuber, J.M. Davis, S.M. Troian, W.W. Reisner, Thermocapillary actuation of liquid flow on chemically patterned surfaces, Phys. Fluids 15 (5) (2003) 1295–1304, https://doi.org/10.1063/1.1562628.

[34] Q. Dai, M.M. Khonsari, C. Shen, W. Huang, X. Wang, Thermocapillary migration of liquid droplets induced by a unidirectional thermal gradient, Langmuir 32 (30) (2016) 7485–7492, https://doi.org/10.1021/acs.langmuir.6b01614.

[35] J. Wang, Flow time measurements for underfills in flip-chip packaging, IEEE Trans. Compon. Packag. Technol. 28 (2) (2005) 366–370, https://doi.org/10.1109/TCAPT.2005.848488.

[36] G. Harvel, B. Komeili, C. Ching, J.S. Chang, Electrohydrodynamically enhanced capillary evaporator, IEEE Trans. Dielectr. Electr. Insul. 16 (2) (2009) 456–462, https://doi.org/10.1109/TDEI.2009.4815178.

[37] M.M. Ohadi, S.V. Dessiatoun, B. Mo, J. Kim, H. Jake), K. Cheung, J. Didion, An experimental feasibility study on EHD-assisted capillary pumped loop, CPL) 567 (2009) 567–572, https://doi.org/10.1063/1.52047. April 2008.

[38] C. Qi, Y. Li, Z. Liu, T. Kong, Electrohydrodynamics of droplets and jets in multiphase microsystems, Soft Matter 16 (37) (2020) 8526–8546, https://doi.org/10.1039/d0sm01357a.

[39] T. Gao, A. Doak, J.M. Vanden-Broeck, Z. Wang, Capillary–gravity waves on a dielectric fluid of finite depth under normal electric field, Eur. J. Mech. B Fluid 77 (2019) 98–107, https://doi.org/10.1016/j.euromechflu.2019.04.007.

[40] P. Azizian, M. Azarmanesh, M. Dejam, M. Mohammadi, M. Shamsi, A. Sanati-Nezhad, A.A. Mohamad, Electrohydrodynamic Formation of single and double emulsions for low interfacial tension multiphase systems within microfluidics, Chem. Eng. Sci. 195 (2019) 201–207, https://doi.org/10.1016/j.ces.2018.11.050.

[41] F. Almasi, M. Hopp-Hirschler, A. Hadjadj, U. Nieken, M.S. Shadloo, Coupled electrohydrodynamic and thermocapillary instability of multi-phase flows using an incompressible smoothed particle hydrodynamics method, Energies 15 (7) (2022), https://doi.org/10.3390/en15072576.

[42] Z. Abbas, D. Wang, Z. Du, K. Zhao, Z. Du, L. Lu, Y. Cui, J. Liang, Numerical simulation of stable electrohydrodynamic cone-jet formation and printing on flexible substrate, Microelectron. Eng. 237 (2021) 111496, https://doi.org/10.1016/j.mee.2020.111496. October 2020.

[43] I. Saad, S. Maalej, M.C. Zaghdoudi, Electrohydrodynamic effects on a nanofluid-filled flat heat pipe, Therm. Sci. Eng. Prog. 16 (2020), 100426, https://doi.org/10.1016/j.tsep.2019.100426. September 2019.

[44] G. Raju, N. Kyriakopoulos, J.V.I. Timonen, Diversity of non-equilibrium patterns and emergence of activity in confined electrohydrodynamically driven liquids, Sci. Adv. 7 (38) (2021) 1–9, https://doi.org/10.1126/sciadv.abh1642.

[45] K. Mohammadi, M.R. Movahhedy, S. Khodaygan, Colloidal particle reaction and aggregation control in the electrohydrodynamic 3D printing technology, Int. J. Mech. Sci. 2021 (195) (2020), 106222, https://doi.org/10.1016/j.ijmecsci.2020.106222.

[46] R. Kumar, A.K. Tiwari, D. Tripathi, A. Mishra, Electromagnetic field induced alterations in fluid flow through lacuno-canalicular system of bone, Int. J. Mech. Sci. 217 (2022), 107036, https://doi.org/10.1016/j.ijmecsci.2021.107036. August 2021.

[47] M.S. Onses, E. Sutanto, P.M. Ferreira, A.G. Alleyne, J.A. Rogers, Mechanisms, capabilities, and applications of high-resolution electrohydrodynamic jet printing, Small 11 (34) (2015) 4237–4266, https://doi.org/10.1002/smll.201500593.

[48] H. Lee, J. Lee, B. Seong, H.S. Jang, D. Byun, Printing conductive micro-web structures via capillary transport of elastomeric ink for highly stretchable strain sensors, Adv. Mater. Technol. 3 (2) (2018) 1–7, https://doi.org/10.1002/admt.201700228.

[49] V. Arasu, S. Hwang, B. Zhang, D. Byun, S.H. Park, 1D fibers and 2D patterns made of quantum dot-embedded DNA via electrospinning and electrohydrodynamic jet printing, Adv. Mater. Technol. 4 (2) (2019) 1–9, https://doi.org/10.1002/admt.201800280.

[50] A. Bandopadhyay, S. Mandal, S. Chakraborty, Streaming potential-modulated capillary filling dynamics of immiscible fluids, Soft Matter 12 (7) (2016) 2056–2065, https://doi.org/10.1039/c5sm02687c.

[51] C.P. Tso, K. Sundaravadivelu, Capillary flow between parallel plates in the presence of an electromagnetic field, J. Phys. D Appl. Phys. 34 (24) (2001) 3522–3527, https://doi.org/10.1088/0022-3727/34/24/317.

[52] A. Bertsch, S. Jiguet, P. Renaud, Microfabrication of ceramic components by microstereolithography, J. Micromech. Microeng. 14 (2) (2004) 197–203, https://doi.org/10.1088/0960-1317/14/2/005.

[53] W.D. Ristenpart, I.A. Aksay, D.A. Saville, Electrically driven flow near a colloidal particle close to an electrode with a faradaic current, Langmuir 23 (7) (2007) 4071–4080, https://doi.org/10.1021/la062870l.

[54] H. Yamamoto, K. Mori, K. Takemura, L. Yeo, J. Friend, S. Yokota, K. Edamura, Numerical modeling of electro-conjugate fluid flows, Sensors Actuators, A Phys. 161 (1–2) (2010) 152–157, https://doi.org/10.1016/j.sna.2010.04.033.

[55] Y. Dai, Z. Zhou, J. Lin, J. Han, Modeling of two-phase flow in rough-walled fracture using level set method, Geofluids (2017), https://doi.org/10.1155/2017/2429796.

[56] T.C. Chen, T.J. Liao, M.C.M. Lee, Manipulation and precise control of colloidal microsphere resonators coupled to a non-planar waveguide, RSC Adv. 5 (80) (2015) 64918–64924, https://doi.org/10.1039/c5ra11428d.

[57] D.F. Zhang, H.A. Stone, Drop Formation in viscous flows at a vertical capillary tube, Phys. Fluids 9 (8) (1997) 2234–2242, https://doi.org/10.1063/1.869346.

[58] A. Gupta, R. Kumar, Flow regime transition at high capillary numbers in a microfluidic T-junction: viscosity contrast and geometry effect, Phys. Fluids 22 (12) (2010), https://doi.org/10.1063/1.3523483.

[59] E. Castillo-Orozco, A. Kar, R. Kumar, Electrospray mode transition of microdroplets with semiconductor nanoparticle suspension/639/166/988/639/925/927/351/123 article, Sci. Rep. 7 (1) (2017) 1–10, https://doi.org/10.1038/s41598-017-05175-6.

[60] J.D. Wehking, R. Kumar, Droplet actuation in an electrified microfluidic network, Lab Chip 15 (3) (2015) 793–801, https://doi.org/10.1039/c4lc00934g.

[61] J.D. Wehking, L. Chew, R. Kumar, Droplet deformation and manipulation in an electrified microfluidic channel, Appl. Phys. Lett. 103 (5) (2013), https://doi.org/10.1063/1.4817008.

[62] R.V. Raghavan, J. Qin, L.Y. Yeo, J.R. Friend, K. Takemura, S. Yokota, K. Edamura, Electrokinetic actuation of low conductivity dielectric liquids, Sensor. Actuator. B Chem. 140 (1) (2009) 287–294, https://doi.org/10.1016/j.snb.2009.04.036.

[63] R. Kumar, A.K. Tiwari, D. Tripathi, A. Mishra, Electromagnetic field induced alterations in fluid flow through lacuno-canalicular system of bone, Int. J. Mech. Sci. 217 (2022), 107036, https://doi.org/10.1016/j.ijmecsci.2021.107036. November 2021.

[64] M.S. Mahmud, A. Alo, B. Farshchian, G.H. Lee, N. Kim, Pulsed laser ablation on polymethylmethacrylate (PMMA) surfaces for capillary driven flows, Surface. Interfac. 31 (2022), 101989, https://doi.org/10.1016/j.surfin.2022.101989.

[65] S. Neunkirchen, Y. Blößl, R. Schledjewski, A porous capillary tube approach for textile saturation, Compos. Sci. Technol. (2022), https://doi.org/10.1016/j.compscitech.2022.109450. No. March.

[66] R.K. Lade, E.J. Hippchen, C.W. Macosko, L.F. Francis, Dynamics of capillary-driven flow in 3D printed open microchannels, Langmuir 33 (12) (2017) 2949–2964, https://doi.org/10.1021/acs.langmuir.6b04506.

[67] J. Cai, T. Jin, J. Kou, S. Zou, J. Xiao, Q. Meng, Lucas-washburn equation-based modeling of capillary-driven flow in porous systems, Langmuir 37 (5) (2021) 1623–1636, https://doi.org/10.1021/acs.langmuir.0c03134.

[68] S. Mukhopadhyay, J.P. Banerjee, S.S. Roy, Effects of liquid viscosity, surface wettability and channel geometry on capillary flow in SU8 based microfluidic devices, Int. J. Adhesion Adhes. 42 (2013) 30–35, https://doi.org/10.1016/j.ijadhadh.2012.12.001.

[69] J.R. Dann, Forces involved in the adhesive process. II. Nondispersion forces at solid-liquid interfaces, J. Colloid Interface Sci. 32 (2) (1970) 321–331, https://doi.org/10.1016/0021-9797(70)90055-X.

[70] L.P. Yeo, B.K. Lok, Q.M.P. Nguyen, C.W. Lu, Y.C. Lam, Selective surface modification of PET substrate for inkjet printing, Int. J. Adv. Manuf. Technol. 71 (9–12) (2014) 1749–1755, https://doi.org/10.1007/s00170-014-5634-9.

[71] H. Cao, C. Amador, X. Jia, Y. Ding, Capillary dynamics of water/ethanol mixtures, Ind. Eng. Chem. Res. 54 (48) (2015) 12196–12203, https://doi.org/10.1021/acs.iecr.5b03366.